

Shape Optimization of Long-Span Translational Free-Form Shell Roofs in Strong Wind Using Multigrid Method and Variable Complexity Model

**Takuzo Yamashita¹, Tomohiko Kumagai², Toshiyuki Ogawa³, Tomoshi Miyamura⁴
and Makoto Ohsaki⁵**

¹National Research Institute for Earth Science and Disaster Prevention, Miki, Hyogo, Japan,
tyamashi@bosai.go.jp

²Tokyo Institute of Technology, Meguro, Tokyo, Japan, kuma@arch.titech.ac.jp

³Tokyo Institute of Technology, Meguro, Tokyo, Japan, togawa@arch.titech.ac.jp

⁴Nihon University, Koriyama, Fukushima, Japan, miyamura@cs.ce.nihon-u.ac.jp

⁵Hiroshima University, Higashi-Hiroshima, Japan, ohsaki@hiroshima-u.ac.jp

Abstract

Shape optimization of the long-span translational free-form shell roofs subjected to strong wind is carried out to minimize the maximum vertical displacement. The three-dimensional (3D) fluid flow analysis is performed to obtain the highly precise dynamic wind load. To reduce large computational cost of the 3D analysis, the multigrid method is employed to solve the pressure Poisson equation. The objective function of this optimization problem is expected to have strong nonlinearity. By using Response Surface Model (RSM), the objective function is approximated as a smooth function so that computational cost for optimization is reduced. Analyses at several experiment points are required to generate the RSM. It is not practical to perform 3D analyses at all experiment points due to huge computational cost. In order to further reduce the computational cost of the 3D fluid flow analysis, the Variable Complexity Model (VCM), which combines high-fidelity and low-fidelity models, is used for generating the RSM. Accuracy of the results obtained by the RSM generated by the VCM is verified in comparison to those obtained by the RSM generated by the 3D analyses. The numerical results show that the computational cost for shape optimization can be drastically reduced with slight error of the objective function by using the VCM.

Keywords: *multigrid method, response surface model, variable complexity model, translational free-form shell*

1. Introduction

Long-span shell roofs are traditionally used for covering large space for arenas, gymnasiums, and so on. Recently, due to the demand for less constructional cost and period, lightweight structures such as membrane structures and spatial frames are preferred to concrete shells. It is important to consider influence of wind action for designing a lightweight space frame structure. In the field of architectural engineering, wind pressure characteristics of structures are investigated by the wind tunnel or computational fluid dynamics simulations. Although long-span spatial structures should be designed mainly against seismic loads, wind loads are likely to be critical to the lightweight spatial structures due to the lack of out-of-plane stiffness. Since wind load strongly depends on a shape of the structure, the responses to the wind are possible to be reduced by finding the optimal shape. Therefore, shape optimization of such a structure in the strong wind is very effectively applied to practical wind-resistance design.

In order to obtain highly precise dynamic wind load, the three-dimensional finite element analysis of fluid flow (hereafter referred to as 3D fluid flow analysis) is a reliable method. For this analysis, however, a huge computational cost is involved in solving the pressure Poisson equation. The conjugate gradient method (CG method) is commonly used for a large-scale linear problem, though the convergence rate is not high enough. By using the multigrid method (MG method) as a preconditioner of the CG method, the computational time of the pressure Poisson equation can be reduced. The authors[1] have improved the computational efficiency of 3D fluid flow analyses around shell structures by applying the MG method in which the 2D mesh is used as a coarse mesh.

It is not easy to solve a multimodal optimization problem based on a sensitivity analysis. Response Surface Model (RSM) is an effective method for such problem because the sensitivity analysis can be easily carried out. RSM is generated by using responses from experiments or analyses, and approximates the objective function. Responses at enough data points are required to approximate the objective function accurately. Thus, it takes enormous computational time to carry out costly analyses such as 3D fluid flow analyses repeatedly for generating RSM. The Variable Complexity Model (VCM), which estimates the responses of a complex high-fidelity model from the responses of an approximate low-fidelity model, can be effectively used to reduce the computational cost in the preliminary optimization process [2-4].

In this study, a fast solution method is proposed for the shape optimization of the translational free-form shell roofs

for minimizing the maximum vertical displacement against wind loads. In this method, the MG method is applied to the 3D fluid flow analyses and approximate objective functions are found by the RSM, where the responses at each experiment point are computed by the VCM. The accuracy of optimal solution and the improvement in computational efficiency by the VCM is verified in comparison to results obtained by the RSM generated by the 3D analyses only.

2. Response Analysis of Shell Roofs Subjected to Strong Wind

2.1. Analytical Model

Consider the long-span translational free-form shell roof subjected to strong wind, as shown in Fig. 1. Bézier curves are utilized to define the shape of the analytical model. Let $\mathbf{q}^0(s) = (q_x^0(s) \ q_z^0(s))$ the α -th order Bézier curve on the x - z plain and expressed by Eq. (1)

$$\mathbf{q}^0(s) = \sum_{i=0}^{\alpha} \mathbf{R}_i B_i^{\alpha}(s) \quad (1)$$

where $\mathbf{R}_i = (R_i^x, R_i^z)$ is a position vector of a control point, $B_i^{\alpha}(i = 0, \dots, \alpha)$ is an α -th Bernstein basis function, and s ($0 \leq s \leq 1$) is a parameter. The roof shape is defined by $\mathbf{q}(s) = (q_x^0(s) \ y \ q_z^0(s))$. Here, let the order of α be equal to five so as to express a moderate curve shape. The fifth Bézier curve is shown in Fig. 2. It is generated by determining positions of six control points.

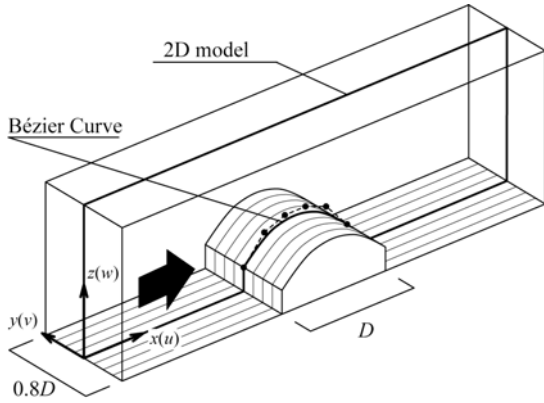


Figure 1. Analytical model

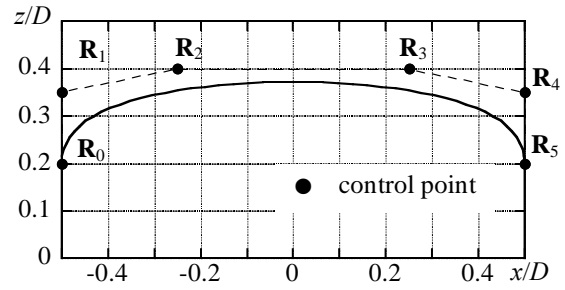


Figure 2. 5th Bézier curve (initial shape)

The x - z section of the mesh at $y = 0$ is illustrated in Fig. 3. The space around the structure is discretized by the finite element method. Linear triangular and tetrahedral elements are used for the 2D and 3D models, respectively. The 3D mesh is generated by dividing each triangular prism, which is generated by extruding a triangle in the y -direction, into six tetrahedrons. The boundary conditions are shown in Table 1. Let u , v , and w denote the wind velocity in the x -, y -, and z -directions, respectively. The velocity u at the inlet boundary has a uniform value of V_H . The turbulent velocity fluctuation, which is stochastically simulated by reflecting the characteristics of the turbulence in the wind tunnel flow, is imposed only in the x -direction. The condition $p = 0$ is given at the outlet boundary in order to prevent singularity of the pressure Poisson equations. In order to prevent a reverse current at the outlet boundary, the viscosity μ is set higher in the domain between $x = 17.5D$ and $20.0D$. The parameters of air are shown in Table 2. The increment of non-dimensional time t^* ($= tV_H/D$) is 0.01. The wind engineering targets the Reynolds number approximately ranging from 7.0×10^4 to 7.0×10^8 . In this study, the value 1.0×10^5 within the semi-critical territory is utilized as a Reynolds number.

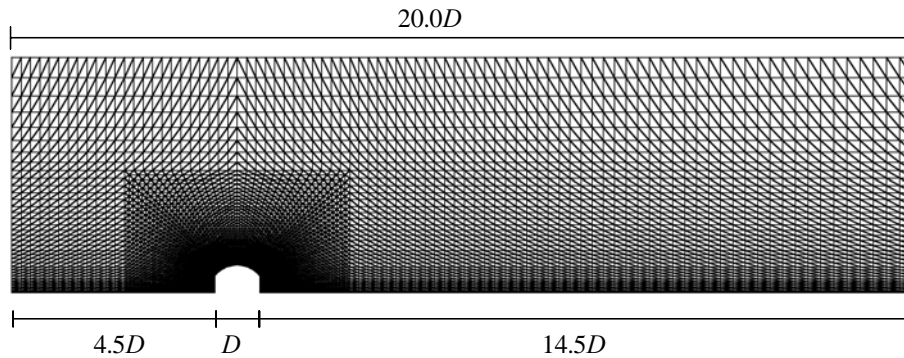


Figure 3. Mesh discretization of space

Table 1. Boundary condition

Inlet	Outlet	Structure surface, Under surface	Upper surface	Side surface
$u=V_H, v=0, w=0$	$p=0$	$u=0, v=0, w=0$	$w=0$	$v=0$

Table 2. Parameter of fluid

Average wind velocity at the inlet boundary V_H (m/sec)	14.5
Density of air ρ_{air} (kg/m ³)	1.25
Coefficient of viscosity μ (N·sec/m ²)	1.81×10^{-5}
Reynolds number Re ($=\rho U_H D / \mu$)	1.0×10^5

Table 3. Model parameter

	Mass per unit area w (kg/m ²)	First natural frequency (Hz)	Span D (m)	Average velocity at reference point V_H (m/s)	Bending stiffness per unit width EI (N·m ² /m)	Mass parameter C_M	Load parameter C_L
Analytical model	8.10×10^{-2}	3.12×10^2	0.1	14.5	2.61×10^{-2}	0.65	5.04
Realistic model	80.0	1.00	100	50.0	2.65×10^8	0.64	5.90

Model parameters are shown in Table 3. The parameters of the analytical model are determined so that the values of mass parameter C_M and load parameter C_L correspond to those of the realistic model. C_M and C_L are expressed by Eqs. (2) and (3), respectively.

$$C_M = w / (\rho_{air} D) \quad (2)$$

$$C_L = Q_H D^3 / (EI) \quad (3)$$

where Q_H is velocity pressure at the reference point.

2.2. Method of Analysis

Outline of 3D fluid flow analysis is explained as below. The governing equations in the present study are the filtered Navier-Stokes equation and the continuity equation. The Navier-Stokes equation discretized in time domain by the Crank-Nicolson method and the continuity equation are expressed by Eqs. (4) and (5), respectively.

$$\frac{\bar{u}_i^{n+1} - \bar{u}_i^n}{\Delta t} + \sum_{j=1}^d \bar{u}_j^n \frac{\partial \bar{u}_i^{n+1/2}}{\partial x_j} + \frac{1}{\rho} \frac{\partial \bar{p}^{n+1/2}}{\partial x_i} - (v + v_{SGS}) \sum_{j=1}^d \frac{\partial}{\partial x_j} \left(\frac{\partial \bar{u}_i^{n+1/2}}{\partial x_j} + \frac{\partial \bar{u}_j^{n+1/2}}{\partial x_i} \right) = 0 \quad (i = 1, \dots, d) \quad (4)$$

$$\sum_{j=1}^d \frac{\partial \bar{u}_j^{n+1/2}}{\partial x_j} = 0 \quad (5)$$

where u ; velocity, p ; pressure, $(\bar{\quad})$; space average, d ; spatial dimension, Δt ; time increment, v ($=\mu/\rho_{air}$); molecule viscosity coefficient, v_{SGS} ; eddy viscosity coefficient, and $u_i^{n+1/2} = (u_i^n + u_i^{n+1})/2$. The superscript n denotes the value at the n -th time-step. The subscripts 1, 2 and 3 denote the x -, y -, and z -components, respectively. The standard Smagorinsky model is employed as an eddy viscosity model with the model coefficient of 0.1.

The discretized Navier-Stokes equation and the pressure Poisson equation are introduced by the improved balancing tensor diffusion method and the fractional step method (IBTD + FS method) combined with the finite element method. In this scheme, equal-order interpolation elements are used for velocity and pressure. The pressure Poisson equation is represented as a large-scale system of linear equations having dimensions that are equal to the number of nodes on the mesh. It was confirmed that the simulated results obtained by the present method agree well with the experimentally obtained results from a wind tunnel test [5].

Response analyses are conducted only for the shell roofs assuming that the walls are considered to be rigid. The edge of the roof and the wall are connected with pin-joint. Roofs are idealized as a 2D model with 49 nodes and 48 linear beam elements on assumption that the roof unlimitedly expands in the y -direction. As a solution method of the motion equation, Newmark- β method ($\beta = 0.25$) is employed. The damping matrix is introduced using Eq. (6)

$$[C] = ([U])^{-1} [\setminus sC \setminus] ([U])^{-1} \quad (6)$$

where U is a mode matrix and sC is an s -th generalized damping coefficient which is determined by the s -th damping factor. The damping factors of the first and second mode are set to 2%, and those of more than third modes are set to 20%. The average pressure along the y -direction at each time step is used as dynamic input load, where fluid-structure interaction is not considered.

2.3. Application of Multigrid Method

For a 3D fluid flow analysis, a huge computational cost is involved in solving the pressure Poisson equation. In this study, the convergence rate of the solution is improved by employing the MG method as a preconditioner of the CG method. The algorithm of the preconditioned CG method (PCG method) is shown in Fig. 4. The PCG method is used to solve the pressure Poisson equation $\mathbf{Ax}=\mathbf{b}$. The MG method is utilized for $\mathbf{e}=\mathbf{M}_{MG}^{-1}\mathbf{d}$ (the subscript i is omitted). The outline of the MG method is shown in Fig. 5. The 2D mesh is used as a coarse mesh. This procedure can be divided into three parts. (I) restriction : mapping the residual \mathbf{d} of the fine mesh on the coarse mesh by averaging the residuals of the nodes aligned in the y -direction. (II) computing the solution on the coarse mesh \mathbf{e}_{coarse} by solving the equation $\mathbf{A}_{coarse}\mathbf{e}_{coarse}=\mathbf{d}_{coarse}$. (III) prolongation : mapping the solution \mathbf{e}_{coarse} on the fine mesh by distributing the value on the coarse mesh to the corresponding nodes on the fine mesh aligned in the y -direction.

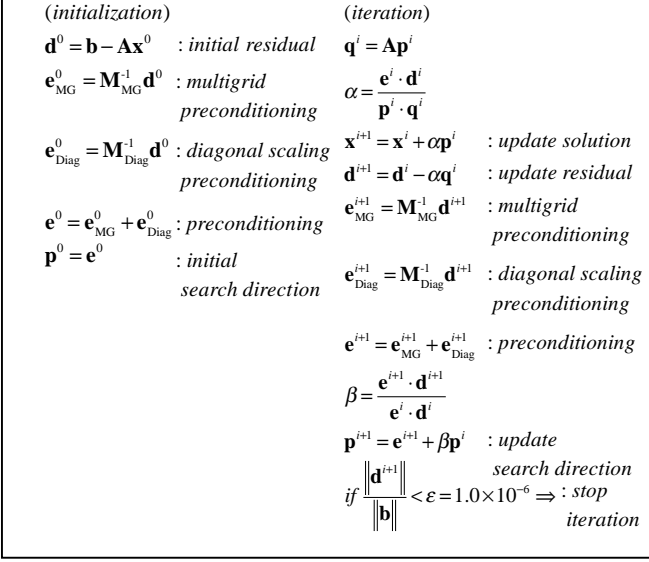


Figure 4. Algorithm of the PCG method

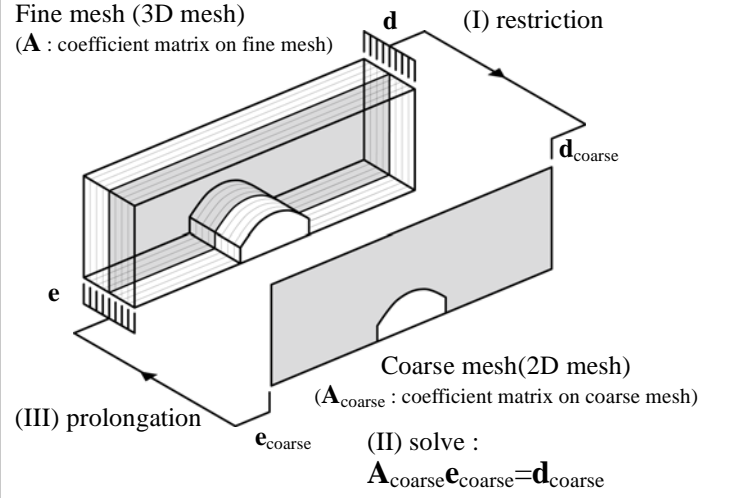


Figure 5. Outline of the MG method

3. Formulation of Shape Optimization Problem

Shape optimization problem of the long-span translational free-form shell roof subjected to strong wind is formulated as follows:

$$\text{Minimize : } f(\mathbf{R}) = \max \{ w^{\max}, -w^{\min} \} \quad (7)$$

$$\text{Variable : } \mathbf{R} = (R_1^z \ R_2^z \ R_3^z \ R_4^z) \quad (8)$$

$$\text{Subject to : } (R_2^z + R_3^z) / 2 \geq 0.4 \quad (9)$$

$$R_i^z \geq 0.2 \ (i = 1, 2, 3, 4) \quad (10)$$

where w^{\max} and $-w^{\min}$ are maximum and minimum value of response displacement in the z -direction of all nodes, respectively. Buildings are generally designed so that maximum response does not exceed the allowable value. Therefore, the objective function is defined as Eq. (7). As shown in Fig. 2, the control points \mathbf{R}_0 and \mathbf{R}_5 are fixed at the tops of windward and leeward side walls, respectively. The z -coordinates of other control points are the design variables (Eq. (8)). The design variables \mathbf{R} of the initial shape shown in Fig. 2 is $(R_1^z \ R_2^z \ R_3^z \ R_4^z) = (0.35 \ 0.4 \ 0.4 \ 0.35)$. Stiffness and weight of members are not included in design variable. Constraints are decided to avoid the shell roof from being low-rise (Eqs. (9) and (10)). However, constraint condition that the roof shape of the windward and leeward side becomes symmetric is not imposed because there are some cases in which the structure is subjected to prevailing wind.

4. Optimization Method

4.1. Response Surface Model

The optimization problem in this study is assumed to be multi-peak problem because the objective function is the maximum response displacement to the dynamic wind load. Thus, in order to reduce the computational cost, RSM is employed as a meta-model so that the sensitivity analysis can be easily conducted. Optimal solution for the objective function generated by the RSM is obtained by using the optimization algorithm called the sequential quadratic

programming provided by the software package DOT Ver. 5.0 [6]. The objective function is approximated by complete quadratic function of the vector $\mathbf{r}=\{r_i\}(-1\leq r_i\leq 1)$ as

$$f \simeq a_0 + \sum_{i=1}^N a_i r_i + \sum_{i=1}^N \sum_{j=i}^N a_{ij} r_i r_j \quad (11)$$

where N is the number of design variables. Relation of the vector \mathbf{r} and the design variable \mathbf{R} is expressed by Eq. (12)

$$\mathbf{R}(\mathbf{r}) = \mathbf{R}^{(k)} + \Delta R \mathbf{r} \quad (12)$$

where $\mathbf{R}^{(k)}$ is optimal solution after k -th step of optimization and an initial value of the next step. The initial value with $k=0$ is design variables at the initial shape. ΔR is a move limit. a_0 , a_i and a_{ij} are the coefficients that are to be determined from the least square method for the responses at the selected data (experiment) points. The number n_c of unknown coefficients a_i , and a_{ij} in Eq. (11) has to be 15 or above because $n_c=(N+1)(N+2)/2$ and N is four in this study. In order to obtain accurate results, 30 experiment points are generated by the function ‘cordexch’ in the statistics toolbox of Matlab that generates 3-level approximation for D-optimality [7] ; i.e., r_i takes one of the values from $\{-1,0,1\}$. The origin (0,0,0) is added and total data points become 31. Optimization flow is summarized as

- 1) Assign initial design variable vector $\mathbf{R}^{(0)}$ and the move limit ΔR . Set $k=0$
- 2) Generate experiment points by using $\mathbf{R}^{(k)}$ and ΔR .
- 3) Compute values of the objective function f in Eq. (7) at each experiment point.
- 4) Generate RSM in Eq. (11) by using the values of f computed in 3)
- 5) Find the optimal solution of RSM and compute $\mathbf{R}^{(k+1)}$ from Eq. (12).
- 6) Let $k \leftarrow k+1$ and update ΔR . If not converged go to 2)

Optimal solution may oscillate if the value of ΔR is large. On the contrary, if the value of ΔR is small, the number of optimization steps may increase or this algorithm may get stuck in a local minimum. Taking it into consideration, we have to replace ΔR successively.

4.2. Variable Complexity Model

It takes huge computational time to conduct the 3D fluid flow analysis repeatedly for the procedure 3) of optimization flow explained in section 4.1. In order to reduce the computational cost, the VCM method, which is the approximate optimization method by using the high-fidelity model and low-fidelity model, is employed. In this study, for the high-fidelity model, the 3D fluid flow analysis is used for computing the wind load. On the other hand, for the low-fidelity model, the 2D fluid flow analysis is used. Hereinafter the analysis for the high-fidelity model and the low-fidelity model are called 3D analysis and 2D analysis, respectively.

The Fourier transformation of the time-history response $\delta_i(t)$ at node i ($i = 1, \dots, 47$) except the both ends is denoted by $\delta_{i\omega}(\mathbf{R})$ as a function of \mathbf{R} . The Fourier spectra from 2D and 3D analyses are denoted by $\delta_{i\omega}^{2D}$ and $\delta_{i\omega}^{3D}$, respectively. The VCM factor $\sigma_{i\omega}(\mathbf{R}^{(k)})$ for design variable is given as follows:

$$\sigma_{i\omega}(\mathbf{R}^{(k)}) = \delta_{i\omega}^{3D}(\mathbf{R}^{(k)}) - \delta_{i\omega}^{2D}(\mathbf{R}^{(k)}) \quad (13)$$

The Fourier spectrum is approximated by using the VCM factor $\sigma_{i\omega}(\mathbf{R}^{(k)})$ as follows:

$$\delta_{i\omega}^{3D}(\mathbf{R}^{(k)} + \Delta R \mathbf{r}) \simeq \delta_{i\omega}^{2D}(\mathbf{R}^{(k)} + \Delta R \mathbf{r}) + \sigma_{i\omega}(\mathbf{R}^{(k)}) \quad (14)$$

The procedure 3) of the optimization flow described in section 4.1 is modified by applying the VCM as follows:

- 3)-1 Conduct both 2D and 3D analyses at initial experiment point $\mathbf{R}^{(k)}$ and compute the VCM factor $\sigma_{i\omega}(\mathbf{R}^{(k)})$ from Eq. (13).
- 3)-2 Compute $\delta_{i\omega}^{2D}(\mathbf{R}^{(k)} + \Delta R \mathbf{r})$ by conducting the 2D analyses at each experiment point and estimate $\delta_{i\omega}^{3D}(\mathbf{R}^{(k)} + \Delta R \mathbf{r})$ from Eq.(14) by using the VCM factor $\sigma_{i\omega}(\mathbf{R}^{(k)})$.
- 3)-3 Compute the time-history responses at all nodes of the shell roof by inverse Fourier transform of $\delta_{i\omega}^{3D}(\mathbf{R}^{(k)} + \Delta R \mathbf{r})$ and obtain objective values at each experiment point.

The 2D mesh used for the VCM is the same as that used as the coarse mesh in the MG method, and the same program can be used in solving the 2D pressure Poisson equation. Thus, the method using both the MG method and the VCM has the advantage of implementation.

As the VCM factor, in addition to the difference model defined by Eq. (13), the ratio model used in reference [3] can be chosen. Then, the accuracies of the difference model and ratio model are compared. The difference in the response between the difference model and ratio model are shown in Fig. 6. Note that in Fig. 6, differences are divided by the average \bar{f}_{3D} of the responses at 31 experiment points. Responses in (a) and (b) are computed at the experiment points, which are generated by using initial value and ΔR of STEP1 and STEP6 listed later in Tables 5 and 6, respectively. In STEP1, the accuracy of the difference model is high. On the other hand, the accuracy of the ratio model is not sufficiently high at several points. In STEP6, both accuracies are worse than STEP1, however, the accuracy of the

difference model does not deteriorate remarkably. For this reason, the difference model is rational and thus is employed in this study as the VCM factor.

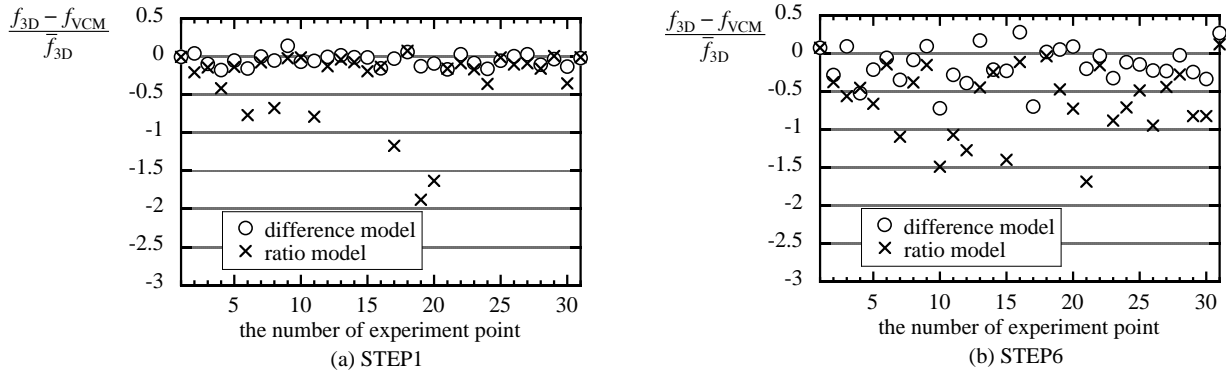


Figure 6. Difference in response between difference model and ratio model

5. Result of Numerical Analysis

Shape optimization of the translational free-form shell is conducted by applying the MG method described in section 2.3. Hereinafter the case in which the RSM is generated by the VCM is called R-VCM and the case in which the 3D analyses are conducted at all experiment points is called R-3D. A total of 1024 data of the time-history responses are sampled from 2885th to 8000th step at every five time steps. For computation, TSUBAME Grid Cluster of Tokyo Institute of Technology Global Scientific Information and Computing Center is utilized. One node has eight dual-core AMD Opteron 880 processors running at 2.4GHz and 32GB of memory. The computational time as shown later in section 5.1 is measured in the occupied node.

5.1. Computational Time

For one optimization step, computational time is occupied mostly by the fluid flow analyses. In R-VCM, 2D and 3D analyses are carried out 31 times and once, respectively, while, in R-3D, 3D analyses are carried out 31 times. At the first optimization step, in order to examine the effect of the VCM, the computational time taken for the 2D analyses at 31 experiment points and the 3D analysis at the initial experiment point $\mathbf{R}^{(0)}$ are measured. Also, in order to examine the effect of the MG method, the computational time for the 3D analysis without the MG method is measured. These computational times are shown in Table 4. From Table 4, it is found that, without the MG method, it takes approximately 17 hours to generate the RSM in R-VCM, and approximately 387.5 hours in R-3D. Therefore, the computation for the optimization problem in R-VCM becomes 22.8 times faster than R-3D. Note that, in R-3D, the computational time to generate RSM is estimated by multiplying the computational time taken for the 3D analysis at initial experiment point $\mathbf{R}^{(0)}$ by 31, which is the number of experiment points. In R-VCM combined with the MG method, computational time to generate the RSM is approximately 10.3 hours. It is reduced to approximately 61%. On the other hand, in the R-3D, by using the MG method, computational time is reduced to approximately 46%. Hence, the computation of the optimization problem becomes far more faster by using the MG method together with the VCM.

Table 4. Computational time for 2D and 3D analyses (first optimization step)

2D analyses at 31 experiment points (hour)	4.5
3D analysis at initial experiment point $\mathbf{R}^{(0)}$ without the MG method (hour)	12.5
3D analysis at initial experiment point $\mathbf{R}^{(0)}$ with the MG method (hour)	5.8

5.2. Result of Optimization

The optimization histories of R-3D and R-VCM are shown in Tables 5 and 6, respectively. The second rows in the Tables 5 and 6 indicate the initial design value $\mathbf{R}^{(0)}$ and the objective value f of $\mathbf{R}^{(0)}$. At STEP1, $\mathbf{R}^{(0)}$ is assigned as an initial value and the move limit ΔR is set to be 0.05, and then the optimal solution is obtained. After STEP1, optimal solution of the former optimization step is assigned as an initial value of the next optimization step, and the move limit ΔR is decrease by half for every two steps. The objective value f of the optimal solution did not oscillate but decreased in the early stage. Therefore, the setting of ΔR is considered to be appropriate. f_{RS} and f are the objective value of optimal solution computed by using the RSM and the 3D analysis, respectively. Compared to f , the error of f_{RS} is found to be small except STEP5 of R-3D.

Table 5. Optimization history of R-3D

STEP	initial value	ΔR	optimal solution	R_1^z	R_2^z	R_3^z	R_4^z	f_{RS}	f
0	---	---	$\mathbf{R}^{(0)}$	0.350	0.400	0.400	0.350	---	8.01×10^{-3}
1	$\mathbf{R}^{(0)}$	5.00×10^{-2}	$\mathbf{R}^{(1)}$	0.300	0.450	0.432	0.300	4.91×10^{-3}	5.35×10^{-3}
2	$\mathbf{R}^{(1)}$	5.00×10^{-2}	$\mathbf{R}^{(2)}$	0.250	0.498	0.466	0.250	1.84×10^{-3}	2.43×10^{-3}
3	$\mathbf{R}^{(2)}$	2.50×10^{-2}	$\mathbf{R}^{(3)}$	0.225	0.473	0.486	0.226	1.75×10^{-3}	1.91×10^{-3}
4	$\mathbf{R}^{(3)}$	2.50×10^{-2}	$\mathbf{R}^{(4)}$	0.200	0.448	0.467	0.201	0.98×10^{-3}	0.90×10^{-3}
5	$\mathbf{R}^{(4)}$	1.25×10^{-2}	$\mathbf{R}^{(5)}$	0.213	0.459	0.470	0.213	0.26×10^{-3}	1.27×10^{-3}
6	$\mathbf{R}^{(5)}$	1.25×10^{-2}	$\mathbf{R}^{(6)}$	0.200	0.447	0.457	0.201	0.95×10^{-3}	0.88×10^{-3}

Table 6. Optimization history of R-VCM

STEP	initial value	ΔR	optimal solution	R_1^z	R_2^z	R_3^z	R_4^z	f_{RS}	f
0	---	---	$\mathbf{R}^{(0)}$	0.350	0.400	0.400	0.350	---	8.01×10^{-3}
1	$\mathbf{R}^{(0)}$	5.00×10^{-2}	$\mathbf{R}^{(1)}$	0.300	0.450	0.450	0.300	4.82×10^{-3}	5.25×10^{-3}
2	$\mathbf{R}^{(1)}$	5.00×10^{-2}	$\mathbf{R}^{(2)}$	0.250	0.500	0.455	0.250	2.80×10^{-3}	2.61×10^{-3}
3	$\mathbf{R}^{(2)}$	2.50×10^{-2}	$\mathbf{R}^{(3)}$	0.226	0.475	0.480	0.225	1.99×10^{-3}	1.93×10^{-3}
4	$\mathbf{R}^{(3)}$	2.50×10^{-2}	$\mathbf{R}^{(4)}$	0.201	0.474	0.495	0.200	1.34×10^{-3}	1.35×10^{-3}
5	$\mathbf{R}^{(4)}$	1.25×10^{-2}	$\mathbf{R}^{(5)}$	0.213	0.462	0.482	0.203	1.20×10^{-3}	1.16×10^{-3}
6	$\mathbf{R}^{(5)}$	1.25×10^{-2}	$\mathbf{R}^{(6)}$	0.203	0.474	0.475	0.209	1.26×10^{-3}	1.24×10^{-3}

The change of the objective value f of the optimal solution is shown in Fig. 7. The changes of f in both R-3D and R-VCM are similar. The results at STEP6 and STEP5 are considered as the optimal solution of the optimization problem in R-3D and R-VCM, respectively. Finally, The objective values in R-3D and R-VCM largely decrease to approximately 11.0% and 15.5% of the initial one, respectively. Thus, the optimization results in both R-3D and R-VCM are useful.

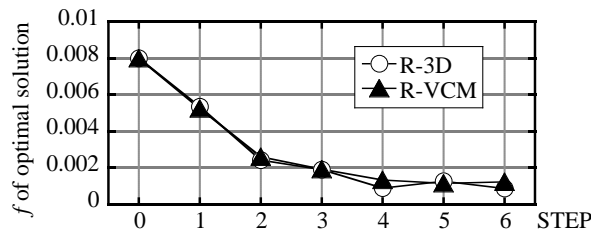


Figure 7. Change of objective value f of optimal solution

To verify the reliability of the optimal solution, the accuracy of the RSM is confirmed by the analysis of variance. The analysis variance is used to linear regression model. Thus, each r_i , r_{irj} ($i \leq j=1,2,3,4$) in Eq. (11) is considered as an independent variable, and the RSM is treated as a linear multi-regression model. The number of the independent variables amounts to 14. The ratio of variance at each optimization step is shown in Fig. 8. Here, A variance ratio F_0 of the vertical axis is expressed in Eq. (15)

$$F_0 = \frac{S_R / p}{S_E / (n - p - 1)} \quad (15)$$

where S_R is the sum of square of the regression model, S_E is that of the error, n is the number of the data points and p is the number of the independent design variables. F_0 indicates how accurately the multi-regression model explains the actual data. $F(0.05,14,16)$ is the value of the F -distribution where significance level is 0.05, $p=14$ and $n-p-1=16$. When the variant ratio F_0 exceeds $F(0.05,14,16)$, this multi-regression model is statistically significant at 95% level of confidence. In this model, RSM expressed by a complete quadratic equation can explain the real objective function sufficiently except the STEP5 of the optimization, and thus the optimal solution obtained by using this model is reliable.

In order to understand how the optimal solution depends on update rule of ΔR at each optimization step, optimizations in these three cases are carried out : the rule employed in Tables 5 and 6 is used in CASE1, the rule with small ΔR is used in CASE2 and the rule with large ΔR is used in CASE3. The influences of the update rule of ΔR on objective values f of optimal solution in R-3D and R-VCM are shown in Figs. 9 (a) and (b), respectively. These changes are almost the same and the optimal solution is not sensitive to ΔR within a range examined here. Therefore, ΔR employed in this example is appropriate.

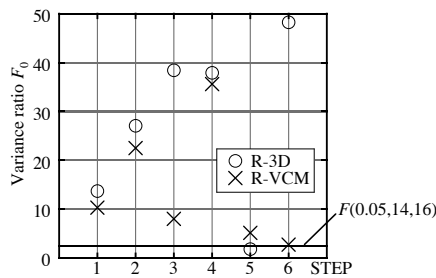


Figure 8. Variance ratio F_0

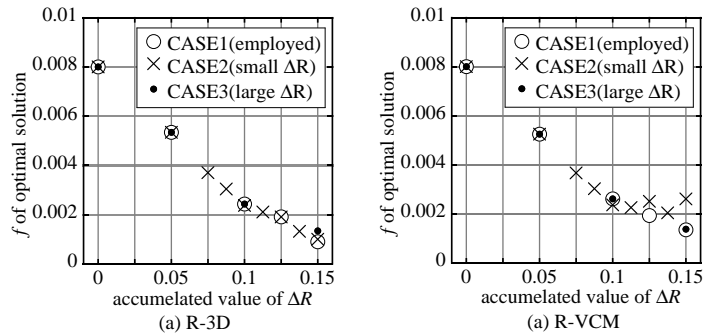


Figure 9. Influence of update rule of ΔR on objective values f

5.3. Verification of Optimal Solution

The initial and optimal shapes in R-VCM and R-3D are shown in Fig. 10 and these curvatures are shown in Fig. 11. The x -coordinates and z -coordinates are non-dimensional dividing by the dome span D in Figs. 10 to 14 (except Fig. 12). The optimal shapes are lower than the initial one in the windward and leeward parts. The rise of the optimal shape in R-3D is lower than that in R-VCM. For the control points of the optimal shape, \mathbf{R}_1 and \mathbf{R}_4 are located over those of initial shape, whereas \mathbf{R}_2 and \mathbf{R}_3 are under the those of initial shape. Distribution of these control points makes the curvature of the optimal shape almost uniform and the optimal shape close to a cylinder.

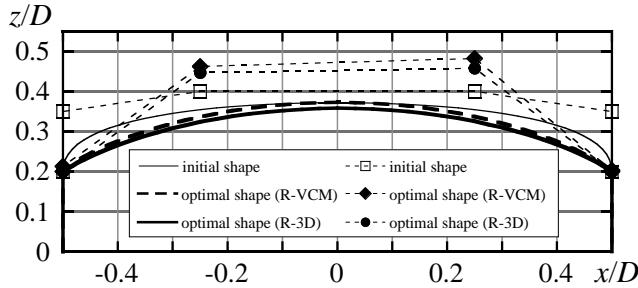


Figure 10. Initial shape and optimal shapes in R-VCM and R-3D

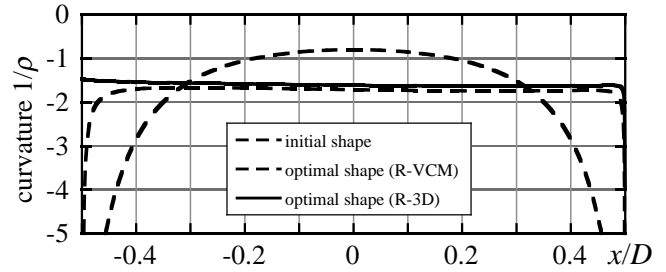


Figure 11. Curvature of initial shape and optimal shapes in R-VCM and R-3D

The pressure contours are shown in Fig. 12 at non-dimensional time $tV_H/D = 60$. Pressure data from Figs.12 to 14 are averaged values of the data aligned in the y -direction. The difference in pressure contour between the initial and optimal shape is that the isobar of the initial shape is denser than that of the optimal shape around the edge of the windward roof surface. There is no definite difference in pressure contour between R-3D and R-VCM for the optimal shape. The same results are observed at the non-dimensional times 20, 40 and 80. The mean wind pressure coefficient C_p and fluctuating wind pressure coefficient C'_p on the roof surface are shown in Figs. 13 and 14, respectively. The pressure data from 2000th to 8000th time step are sampled to compute the wind pressure coefficients. The gradient of C_p for the optimal shape is shallower than that for the initial one on the windward side because the isobars of the optimal shape are sparser than the initial one around there. The peak values of C_p for the optimal and initial shape are almost the same, however, the peak for the optimal shape is located nearer to the center of the roof. The fluctuating wind pressure C'_p for the initial shape is larger than the optimal one on the windward side around which the isobars of the initial shape are denser. There is no definite difference in C_p and C'_p between R-3D and R-VCM.

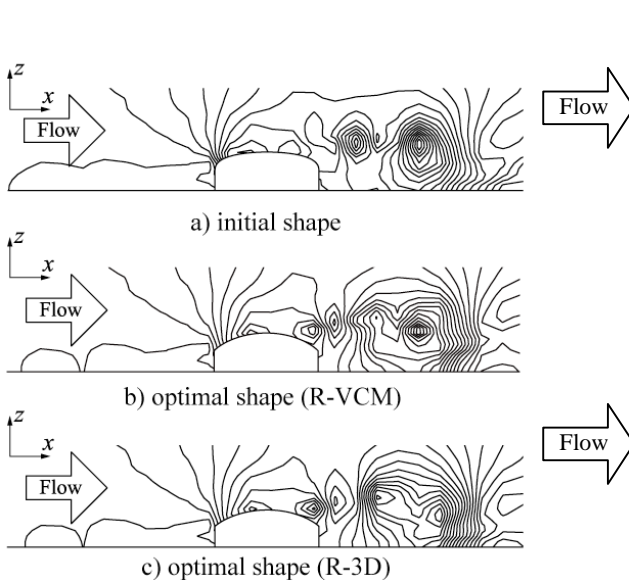


Figure 12. Pressure contour ($tV_H/D = 60$)

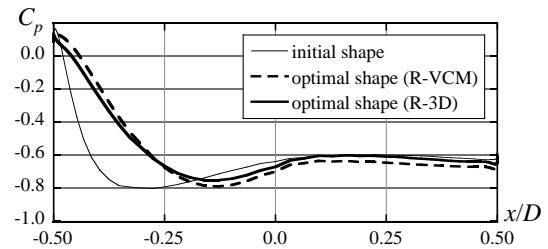


Figure 13. Mean pressure coefficient C_p

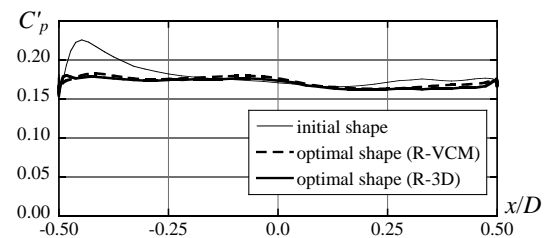


Figure 14. Fluctuating pressure coefficient C'_p

6. Conclusions

Shape optimization of the long-span translational free-form shell subjected to strong wind has been carried out for minimizing the maximum vertical response displacement among all nodes. In the proposed method, to improve

computational efficiency for the shape optimization problem, the multigrid method (MG method) is employed to the three dimensional fluid flow analyses. The Variable Complexity Model (VCM) is also employed to generate the Response Surface Model(RSM). The effects of the MG method and the VCM on the computational efficiency are examined. The conclusions obtained from this study are shown as follows:

- 1) As a model of the VCM factor, the model defined by the difference of the high-fidelity model and the low-fidelity model is appropriate compared to that defined by the ratio.
- 2) Computation for the optimization in the case that the RSM is generated by the VCM (R-VCM) is approximately 22.8 times faster than in the case that the RSM is generated by the three-dimensional fluid flow analyses (R-3D) only. In addition, computational times for the optimization in R-VCM and R-3D are decreased largely by applying the MG method, that is, they are reduced to approximately 61% and 46%, respectively.
- 3) Objective values of the optimal solution in R-VCM and in R-3D are approximately 15.5 % and 11.0% of the initial one, respectively. Hence, both methods are useful for the optimization.
- 4) The optimal shape has uniform curvature; that is, the shape is close to cylinder.
- 5) The gradient of mean wind pressure coefficient C_p for the optimal shape is shallower than that for the initial one. The peak value of C_p for the optimal shape is almost equal to that for the initial one. However, the peak for the optimal shape is located nearer to the center of the roof compared to the initial one. On the other hand, any peak of the fluctuating wind pressure coefficient C_p' is not observed for the optimal shape, whereas a peak is observed for the initial shape on the windward side of the roof.

References

1. T. Yamashita, T. Kumagai, T. Miyamura, T. Ogawa and M. Ohsaki, Application of the Multigrid method to finite element analysis of fluid flow around domes in strong wind, *J. Int. Assoc. Shell and Spatial Struct.*, Vol. 50, No.3, pp. 181-191, 2009.
2. M. G. Hutchinson, E. R. Unger, W. H. Mason, B. Grossman and R. T. Haftka, Variable-complexity aerodynamic optimization of a high-speed civil transport wing, *J. Aircraft*, Vol. 31(1), pp. 110-116, 1994.
3. E. R. Unger, M. G. Hutchinson, M. Rais-Rohani, R. T. Haftka and B. G. Grossman, Variable-complexity multidisciplinary design of a transport wing, *Int. J. System Automation: Research and Appl.*, Vol. 2, pp. 87-113, 1992.
4. H. Hasegawa and S. Sakai, A simulation of the approximate optimization for crash analysis by using the variable complexity modeling, *Trans. of JSCEs*, Paper No. 20030003, Vol. 5, pp. 125-130, 2003.
5. T. Ogawa, K. Nakayama, K. Masuda, and I. Mochizuki, Numerical simulation and experimental study on dynamic behavior of cylindrical dome roofs in strong wind, *Proc. IASS 40th Anniversary Congress*, Vol. 2, 1999, E1.71-E1.80.
6. DOT User's Manual, Ver 5.0, VR&D, 1999.
7. W. J. Roux, N. Stander, and R. T. Haftka, Response surface approximations for structural optimization, *Int. J. Numerical Methods in Engineering*, Vol. 42, Issue 3, pp. 517-534, 1998